Supporting Information for "Extreme curvature of shallow magma pathways controlled by competing stresses"

Timothy Davis[1], Marco Bagnardi[2,3], Paul Lundgren[3], Eleonora Rivalta[1,4]

[1]GFZ (GeoForschungsZentrum), Physics of Earthquakes and Volcanoes, Helmholtzstraße 6/7, Building H 7, 14467 Potsdam, Germany. {davis,rivalta}@gfz-potsdam.de

[2]Now at Cryospheric Sciences Laboratory, NASA Goddard Space Flight Center, 8800 Greenbelt Road, Greenbelt, MD, United States. marco.bagnardi@nasa.gov

[3]Jet Propulsion Laboratory, California Institute of Technology, 4800 Oak Grove Drive, Pasadena, CA, United States. paul.r.lundgren@jpl.nasa.gov

[4]Department of Physics and Astronomy, Alma Mater Studiorum University of Bologna, V.le Berti Pichat 6, Italy. eleonora.rivalta@unibo.it

Contents of this file

Introduction

This document provides the supporting figures and analysis showing how we:

1. Processed the InSAR images

2. Fitted rectangular dislocations to explain the source geometry causing the ground deformation.

3. Used this source geometry to obtain parameters for use in the analytical model.

4. Computed stress intensity factors for a constant volume crack beneath a half-space.

5. Tested the analytical assumption of a penny-shaped crack and its effect on K.

Text S1.

1. Supporting text and figures

1.1. InSAR processing and additional observations

All interferograms were created using the InSAR Scientific Computing Environment (ISCE) software (Rosen et al., 2015) that applies conventional differential InSAR processing techniques for stripmap, ScanSAR (ALOS-2), and Terrain Observation by Progressive Scans (TOPS) (Sentinel-1) data. Topographic contributions to the interferometric phase are removed using the Deutsches Zentrum für Luft und Raumfahrt (DLR) 12-m resolution digital elevation model based on TanDEM-X satellite measurements (Wessel et al., 2018), and interferograms are phase-unwrapped using the Statistical-cost, Network-flow Algorithm for Phase Unwrapping (SNAPHU) implemented in ISCE (Chen & Zebker, 2001).

1.2. InSAR inversions along track

Deformation source parameters and uncertainties are estimated using a Bayesian approach implemented in the Geodetic Bayesian Inversion Software (Bagnardi & Hooper, 2018). The inversion algorithm samples posterior probability density functions (PDFs) of source parameters using a Markov chain Monte Carlo method, incorporating the Metropolis-Hastings algorithm, with automatic step size selection. Posterior PDFs are calculated considering errors in the InSAR data, which we directly quantify using experimental semivariograms to which we fit an unbounded exponential one-dimensional function with a nugget (Bagnardi & Hooper, 2018). The exponential function is then used to populate the data variance-covariance matrix. Prior to inversions, all InSAR data sets are subsampled using an adaptive quadtree sampling (Decriem et al., 2010) to reduce the computational burden when calculating the inverse of the data variance-covariance matrix and in forward model calculations. For all models, we assume that the deformation sources are embedded in an isotropic elastic half-space with Poisson's ratio $\nu = 0.25$. Since no detailed prior information on the deformation source parameters are available, prior probability distributions are assumed to be uniform between geologically realistic bounds. In each inversion, posterior PDFs are sampled through 10^6 iterations. Depth estimates are referred to as distance from the surface.

At profile locations P1, P4 and P5 in Fig. S2 we estimate source parameters of a rectangular dislocation with constant opening (Okada, 1985) and retrieve openings of 0.74±0.03, 1.73±0.03 and 2.80±0.03 m respectively, where the value after ± brackets the 2.5 and 97.5 percentile of the results from our Bayesian inversion scheme (Bagnardi & Hooper, 2018) (Table. S1). Using such solutions the depth of this sill along its path is

consistently 900-1000 m below the ground surface with a half-width of approximately 1.5 km.

1.3. Choosing physical parameters

We approximate the sill in our analytical analysis as a penny shaped crack. To retrieve radius c and volume V for this geometry, we compare the ground deformation of a flat lying rectangular dislocation where the faces open 2 m with a depth d of 950 m and its third axis extending far out of the plane of observation, to the the analytical solution describing the uplift due to a pressurised penny-shaped crack under a half-space with the same d (Sun, 1969). The penny-shaped crack's ground deformation supplies a radial deformation pattern, therefore we only fit this to the ground deformation relative to the short-axis of the sill. Once fitted, we retrieve a radius c= 1900 m and volume $V = 1.6\pi c^2$ (with the largest error 1.5% and 15% less than the maximum u_z and u_x value from the dislocation solution, respectively).

1.4. Comparison of different effects on stress intensity factors

Fig. S4 is computed using a numerical scheme to evaluate how K_I in equation 3, decreases as the crack approaches the free surface (Davis et al., 2019). For c/d=2 as observed, a dip of 15° causes a relative increase and decrease of K_I of +30% and -10% at its highest and lowest edge respectively. A 30% increase corresponds to the same K_I increase as a sill dip of around 15° due to $(\rho_r - \rho_f)g\sin(\beta)$. As with buoyancy, this effect increases with crack dip.

1.5. Approximating the sill geometry as a penny

Here we estimate the error associated with approximating a 3D propagating crack as penny-shaped. We compare analytical formulas that describe K around the tip-line of penny-shaped cracks under uniform pressure and linear stress gradients, equation 3 & 4 to those of a more realistic 3D shape (Fig. S6a). We apply boundary conditions so that the opening of lengthened-tail crack matches that of the penny-shaped crack, at the location where the penny's opening is maximal. For penny-shaped cracks with constant internal pressure this is the crack centre. For a penny-shaped crack under a linear stress gradient the maximal opening is located along the direction of the stress gradient at $\sin(\pi/4)c$. We find the analytical formulas capture the scale and shape of the problem with some deviations (Fig. S6b, c and d). Note the accuracy of the numerical boundary element method to approximate K can have errors of up to 10% and the mesh used in Fig. S6 has ∼2000 triangles (Davis et al., 2019, 2020).

1.6. Free surface effects

To quantify the effects of the free surface on the crack, we use the same input parameters as those for the simulation in Fig. 4 but remove all stresses and buoyancy forces acting on the faces of the crack apart from the internal fluid pressure. We reduce K_c to 1 MPa·m$^{0.5}$ such that the crack can reach the surface. The aim of this test is to see how the crack grows and responds to the free surface in our simulation. Fig. S7 shows its influence when this is flat-lying. Here the crack grows into an axi-symmetric bowl like form. Fig. S8 tests this for the same start geometry we use in our full simulation, and angles the free surface to match the topographic slope. In this simulation the crack reaches the surface at the location where the free surface was originally closest to the start geometry.

References

Bagnardi, M., & Hooper, A. (2018). Inversion of surface deformation data for rapid estimates of source parameters and uncertainties: A bayesian approach. *Geochemistry, Geophysics, Geosystems*, *19*(7), 2194–2211.

Chen, C. W., & Zebker, H. A. (2001). Two-dimensional phase unwrapping with use of statistical models for cost functions in nonlinear optimization. *JOSA A*, *18*(2), 338–351.

Davis, T., Healy, D., & Rivalta, E. (2019). Slip on wavy frictional faults: Is the 3rd dimension a sticking point? *Journal of Structural Geology*, *119*, 33–49. doi: 10.1016/j.jsg.2018.11.009

Davis, T., Rivalta, E., & Dahm, T. (2020). Critical fluid injection volumes for uncontrolled fracture ascent. *Geophysical Research Letters*, e2020GL087774.

Decriem, J., Árnadóttir, T., Hooper, A., Geirsson, H., Sigmundsson, F., Keiding, M., ... others (2010). The 2008 may 29 earthquake doublet in sw iceland. *Geophysical Journal International*, *181*(2), 1128–1146.

Okada, Y. (1985). Surface deformation due to shear and tensile faults in a half-space. *Bulletin of the seismological society of America*, *75*(4), 1135–1154.

Rosen, P., Gurrola, E., Agram, P. S., Sacco, G. F., & Lavalle, M. (2015). The insar scientific computing environment (isce): A python framework for earth science. *AGUFM*, *2015*, IN11C–1789.

Savage, W. Z., Powers, P. S., & Swolfs, H. S. (1984). *In situ geomechanics of crystalline and sedimentary rocks; part v, rvt, a fortran program for an exact elastic solution for*

tectonics and gravity stresses in isolated symmetric ridges and valleys (Tech. Rep.). Denver, Colorado: US Geological Survey,.

Sun, R. J. (1969). Theoretical size of hydraulically induced horizontal fractures and corresponding surface uplift in an idealized medium. *Journal of Geophysical Research*, *74*(25), 5995–6011.

Wessel, B., Huber, M., Wohlfart, C., Marschalk, U., Kosmann, D., & Roth, A. (2018). Accuracy assessment of the global tandem-x digital elevation model with gps data. *ISPRS Journal of Photogrammetry and Remote Sensing*, *139*, 171–182.

Figure S1. Vertical GPS movement's from continuous GPS stations GV01, 02 and 04 situated on Sierra Negra's summit. See Fig. 1 for station location. Data downloaded from `http://geodesy.unr.edu`

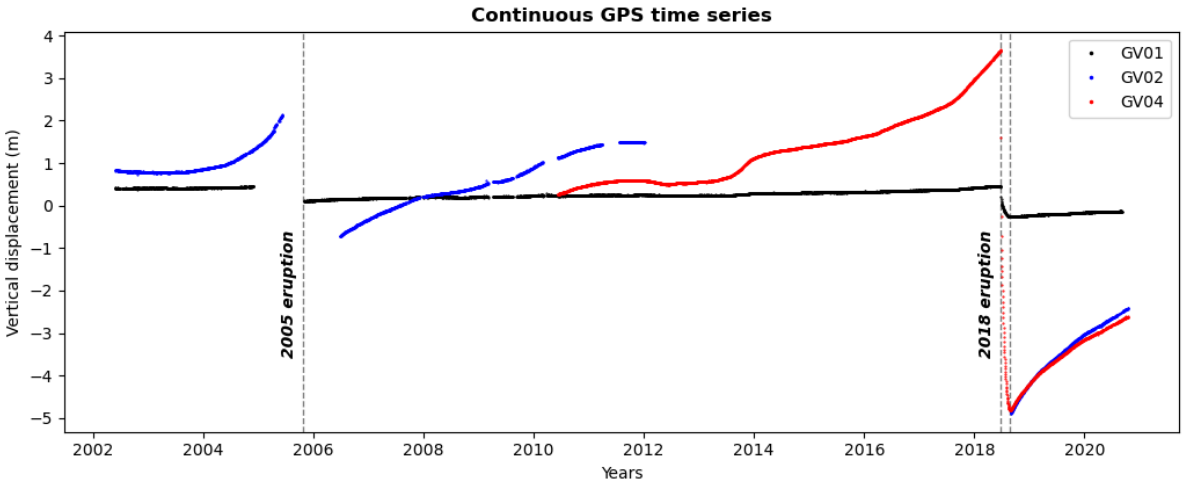

Figure S2. Profiles used to estimate intrusion geometry. a) InSAR as in Fig. 2c) with the location of the profiles (P1 - P7) marked by blue shading. Gray polygons show the extent of the lava flows emplaced during the time period spanned by the interferogram. Yellow lines mark the location and extent of all eruptive fissures. b) Each plot shows the line-of-sight ground displacement for each data point included in profiles 1-7. Vertical scale is not constant. c) As in b) but all profiles have a constant vertical scale, ($\sim$ W-E).

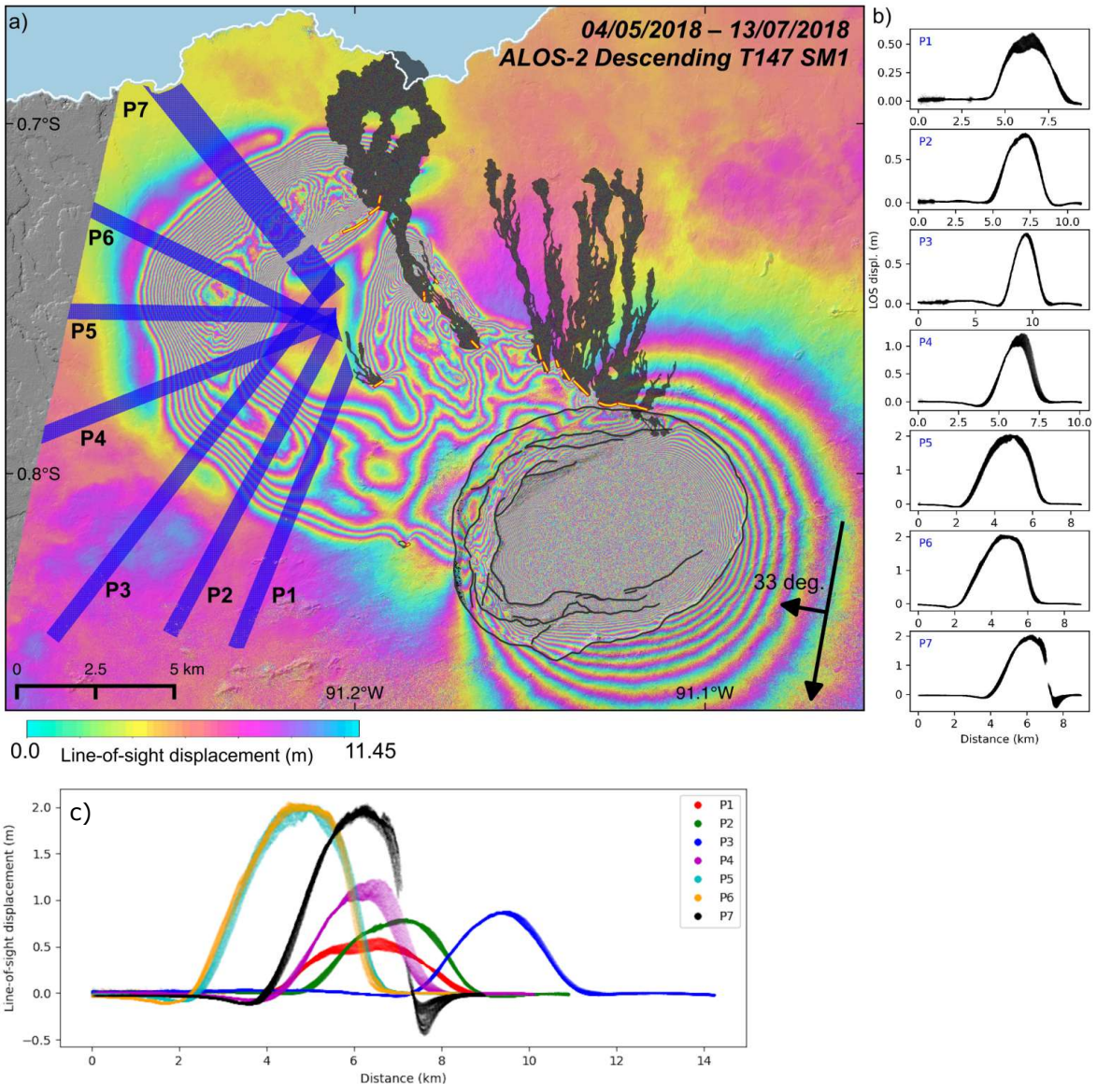

Profile	Opening [m]	Dip°	Dip Direction°	Depth [m]	Down-dip width [m]	Along-strike width [m]
P1	0.7/0.7/0.8	0.6/1.6/2.7	19/21/23	861/899/958	2907/2949/2986	2554/3175/4503
P2	1.0/1.0/1.0	11.0/12.8/15.4	136/140/142	998/1058/1335	2527/2637/3787	2356/2387/2421
P3	1.2/1.2/1.2	3.0/5.5/7.5	138/140/142	939/992/1040	3541/3891/13903	2119/2140/2172
P4	1.7/1.8/1.8	16.7/17.4/18.1	199/199/200	1053/1084/1115	3296/3604/3653	1754/1771/1789
P5	2.8/2.8/2.8	14.0/14.5/15.0	210/210/210	994/1010/1026	2196/2210/2224	2838/2850/2859
P6	2.80/2.83/2.85	14.1/14.6/14.9	352/353/353	976/993/1007	2322/2340/2353	2826/2840/2851

Table S1. Bayesian inversion results for profiles shown in Fig. S2, using rectangular dislocations (Okada, 1985). The 2.5 percentile value, the maximum a posteriori probability solution, and the 97.5 percentile value are shown for each parameter. The results for P7 are not shown, due to unsatisfactory fits to the data.

Figure S3. Magnitude of stress gradients, topographic vs buoyancy. Top panel shows in black the topographic profile of the volcano (profile A-A' in Fig. 3) and in blue an approximation of this profile used to calculate the analytical solution (Savage et al., 1984). Bottom panel shows the required crack dip β such that the two competing gradients match, according to $(\rho_r - \rho_f)g\sin(\beta) = \delta\sigma_v/\delta h$. Plane strain boundary element method result due to the topography is shown in black, the result of the analytical solution (Savage et al., 1984) due to the approximate slope shown is shown in blue.

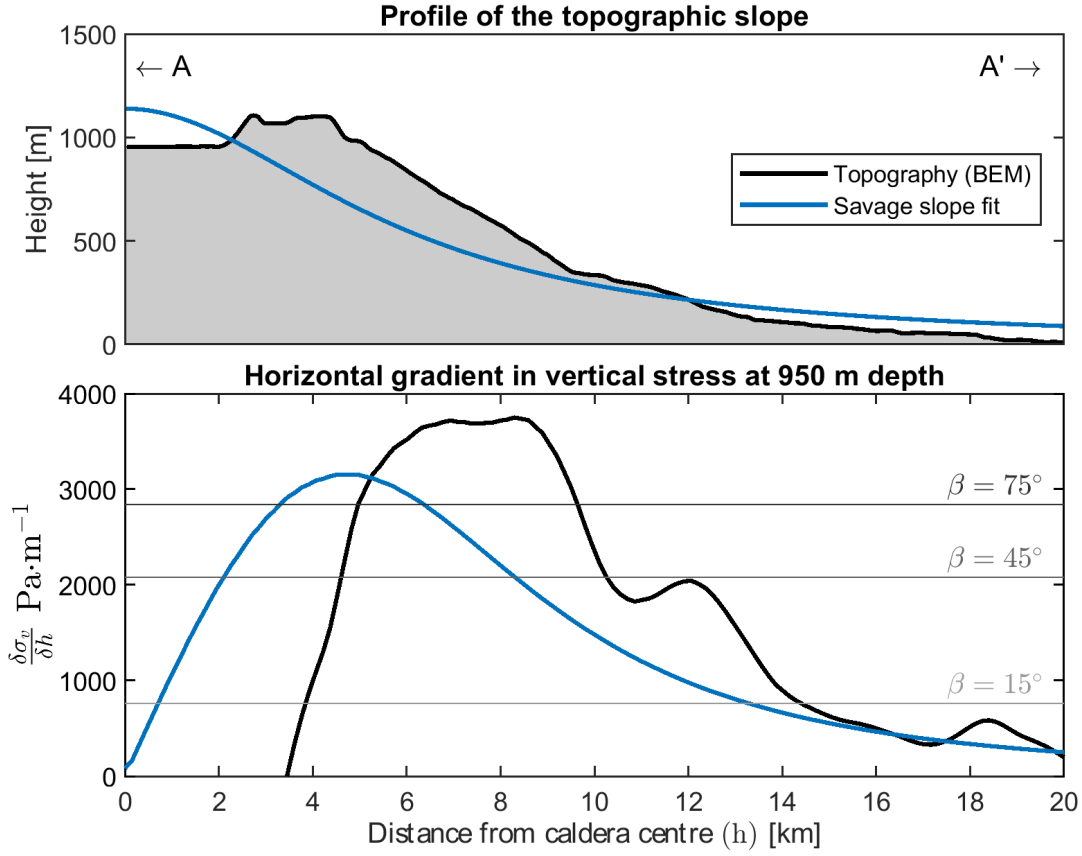

Figure S4. Half-space effects on K_I at the upper and lower tips of a dipping penny-shaped crack. Maximum and minimum K_I values (solid and dashed) for constant volume cracks, depth d below a half-space, with radius c. Values relative to K_∞, equation 3. Note the offset from 1 when c/d=0, indicates the size of the numerical error.

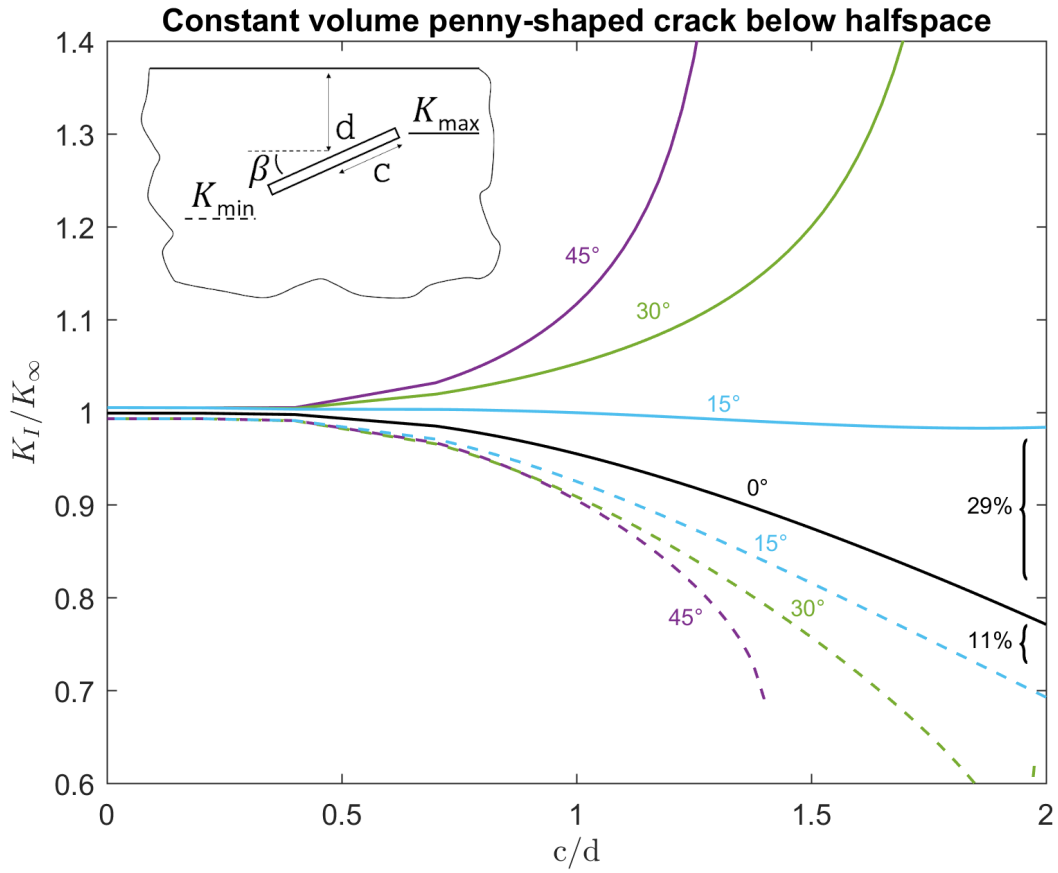

Figure S5. Summary of changes in K due to different effects on the sill at Sierra Negra. Cross sections of cracks showing changes in stress intensity, K_I, at the crack tip due to different processes. Crack opening exaggerated by 300, red patches show the 2nd invariant of stress computed from K at the tip. a) crack in a full space, b) crack under topographic stress gradient, topography exaggerated, c) crack with 15° dip, buoyancy as defined in text, d) interacting cracks with separation defined in text, e) flat crack close to the free surface, f) crack close to free surface with dip, only internal pressure.

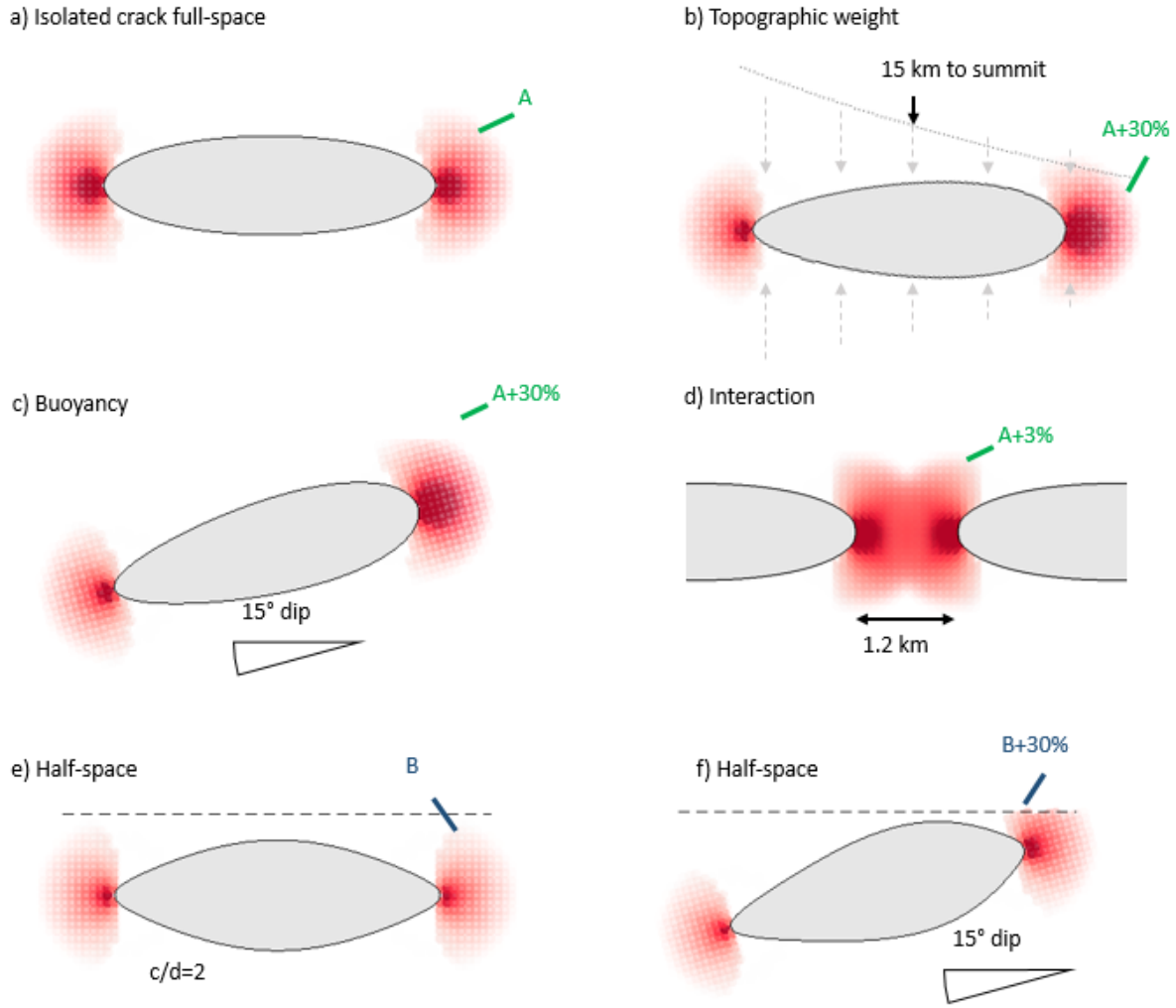

Figure S6. Comparison of K_I around a penny-shaped and elongated penny-shaped crack. a) The mesh used for this analysis. θ is defined in degrees away from the tip ($y = 1$). Comparison of K_I from equation 4 to that for an elongated penny-shaped crack as in a), assuming b) a stress gradient along the x-axis; c) a stress gradient along the y-axis. d) Comparison of K_I from equation 3 to that for an elongated penny-shaped crack with uniform pressure. Note some slight numerical inaccuracies are present.

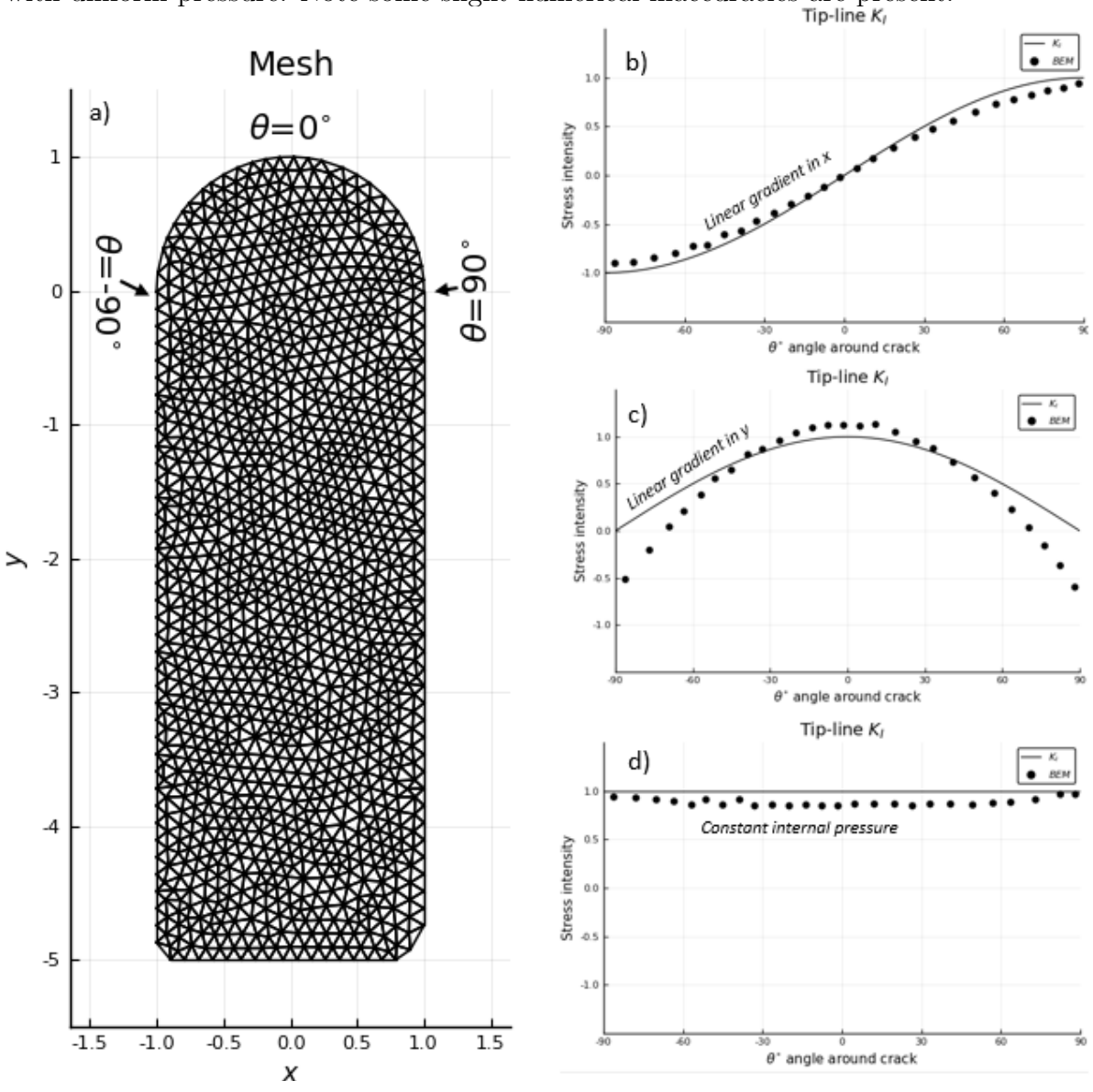

Figure S7. Simulation of a sill growing beneath a flat free surface (dashed line on right hand plot). Stress intensity around the tip-line is shown in the colourbar (MPa·m$^{0.5}$). Sill started as a flat circular crack with a radius of 1900 m, at a depth of 1200 m.

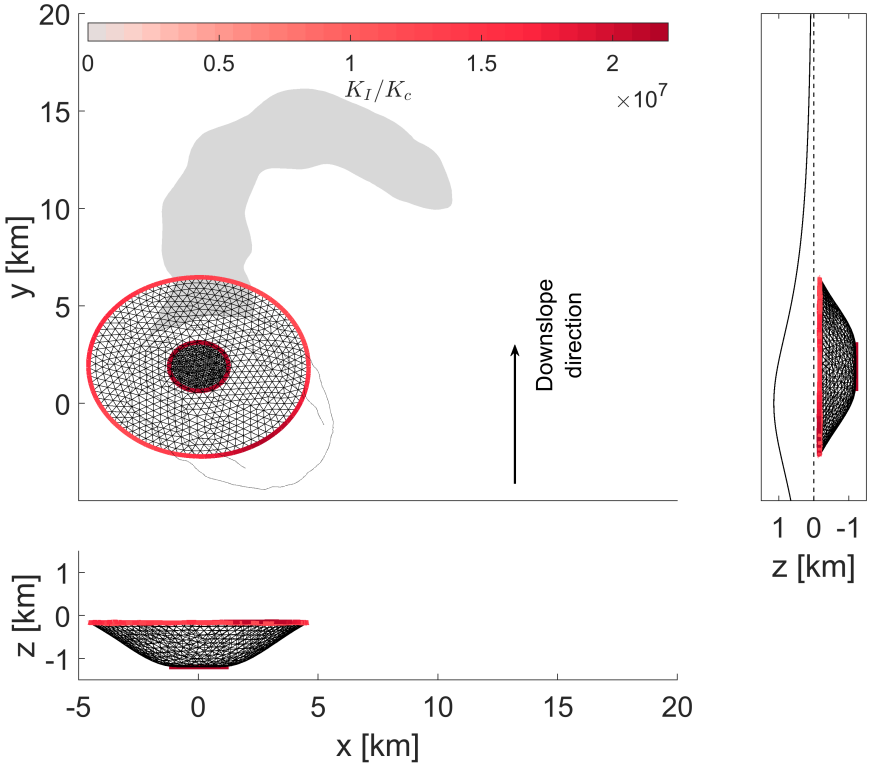

Figure S8. Simulation of a sill growing beneath a dipping free surface (dashed line on right hand plot). Stress intensity around the tip-line is shown in the colourbar (MPa·m$^{0.5}$). Sill started as a flat crack (shown), at a depth of 1200 m.